Complex Coefficient Active Disturbance Rejection Controller for Current Harmonics Suppression of IPMSM Drives

Fan Yang, *Student Member, IEEE*, Feng Jiang, *Student Member, IEEE*, Zhijie Xu, Lingfeng Qiu, Baichuan Xu, Yahui Zhang, and Kai Yang, *Member, IEEE*

***Abstract*—Conventional active disturbance rejection controller (ADRC) for interior permanent magnet synchronous motor (IPMSM) drives suffers deteriorated performance in dealing with low-order harmonic disturbances. To enhance the capability of ADRC in rejecting such disturbances, this article proposes a complex coefficient active disturbance rejection controller (CCF-ADRC). The complex coefficient filter (CCF), which is capable of extracting signals with selective frequency and selective phase sequence from the input orthogonal signals, is incorporated into the extended state observer to enhance its estimation accuracy on the *d-q*-axis harmonic disturbances. With the harmonic disturbances accurately estimated, the subsequently designed CCF-ADRC can achieve enhanced performance in rejecting such disturbances. Theoretical analysis on the stability, the harmonics rejection capability, the command tracking capability, and the influence of parameter mismatches are systematically conducted. Comprehensive experiments on a 1.0-kW IPMSM verify the effectiveness of the proposed method.**

***Index Terms*—Active disturbance rejection control (ADRC), complex coefficient filter (CCF), current harmonics suppression, interior permanent magnet synchronous motor (IPMSM).**

I. Introduction

INTERIOR permanent magnet synchronous motors (IPMSMs) are increasingly used in household and industrial applications due to their high efficiency, high energy density, and high reliability [1]–[2]. In the typical field-oriented control topology for IPMSM, the ideal phase current should be sinusoidal waveform so as to reach desired steady-state performance. However, in a practical IPMSM drive, there exists various current harmonics. To maintain good steady-state performance, it is necessary to suppress the influence caused by such harmonics [3], [4].

The main harmonic components in IPMSM drive system that affect the steady-state performance of the motor are the low-order harmonics, especially the fifth- and seventh-order harmonics, which are commonly induced from inverter nonlinearities [4], [5]. Besides, there are other factors that can cause low-order current harmonics, including nonideal motor design (winding distribution [6], magnetic circuit saturation effect [7], rotor pole structure [8]), unbalanced phase impedances [9], current measurement error [10], [11], and other factors.

Till date, various methods have been put forward to suppress the current harmonics of IPMSM, which can be generally divided into two categories. The first category is to suppress harmonics using feedback controller. For example, the repetitive controller [12], the resonant controller [13]–[15], and the multiple synchronous rotating frame transformation method [16]. In [15], the PI-regulator with a resonant controller (PIR) is applied in the direct torque control to reduce the second- and sixth-order torque and flux harmonics. In [17], an adaptive linear neuron-based current harmonics suppression method is proposed to suppress current harmonics of PMSM with nonsinusoidal back electromotive force. In [18], a novel model predictive torque control is proposed to suppress current harmonics of dual three-phase PMSM. In [19], a robust iterative learning controller achieved by an adaptive sliding mode control technique is proposed to reduce the torque harmonics of the servo system. In [20], a fractional-order vector resonant controller is applied to reduce the current harmonics and improve the robustness to parameter mismatches.

The second category concentrates on estimating and compensating the harmonic disturbances [21]–[30]. Among these methods, ADRC shows great prospects due to its unique advantages in handling systems with various uncertainties and disturbance. ADRC is a composite controller, which is composed of a transient profile generator, a tracking differentiator, and an extended state observer (ESO) [23]–[25]. In [26], an ADRC-based method is developed to eliminate the current harmonic disturbances for the dual three-phase IPMSM drive system.

Manuscript received December 30, 2021; revised March 16, 2022; accepted April 7, 2022. Date of publication April 19, 2022; date of current version May 23, 2022. This work was supported in part by the National Key R&D Program of China under Grant 2018YFB0904800, in part by the National Natural Science Foundation of China under Grant 51677078, and in part by the Science Technology and Innovation Commission of Shenzhen Municipality under Grant JCYJ20170307160832442. Recommended for publication by Associate Editor A. Muetze. *(Corresponding authors: Kai Yang; Feng Jiang.)*

The authors are with the State Key Laboratory of Advanced Elec-tromagnetic Engineering and Technology, School of Electrical and Electronic Engineering, Huazhong University of Science and Technology, Wuhan 430074, China, with the Engineering Research Center of Novel Electrical Machines and Special Electromagnetic Equipments, Ministry of Education, Wuhan 430074, China, and also with the Shenzhen Huazhong University of Science and Technology Research Institute, Shenzhen 518000, China (e-mail: fang_yang@hust.edu.cn; jiangfeng@hust.edu.cn; 17863935734@163.com; 18124856632@163.com; 836018089@qq.com; zhangyahui@hust.edu.cn; yk@mail.hust.edu.cn).

Color versions of one or more figures in this article are available at https://doi.org/10.1109/TPEL.2022.3168367.

Digital Object Identifier 10.1109/TPEL.2022.3168367

Unfortunately, conventional ADRC suffers deteriorated Performance in dealing with low-order harmonic disturbances. As illustrated in [27], ESO can ensure the asymptotic convergence only in dc disturbances estimation. However, when dealing with the harmonic disturbance, due to the limited bandwidth, ESO will suffer significant steady-state estimation error [28]. A higher bandwidth may help to reduce the estimation error, but the observer's sensitivity to noise would be increased, which is not acceptable.

To address the above problems, many solutions have been proposed. In [28], a generalized integrator ESO (GI-ESO) based GI-ADRC is proposed to suppress harmonic disturbances of grid-connected converter. In [29], ADRC is combined with a repetitive controller to suppress the harmonic disturbances. In [30] and [31], the vector resonant controller and the quasi-resonant controller are, respectively, incorporated into the control law of conventional ADRC to improve its harmonic suppression capability. In [32], a high-order ESO is proposed, which offers better state estimation accuracy than the conventional low-order ESO when dealing with time-varying disturbances. The abovementioned methods can suppress harmonic disturbances with selective frequencies. However, they have a common drawback. In a practical IPMSM drive system, the d-q-axis current harmonics do not just have frequency differences, they have phase sequence differences. For example, the harmonic disturbance caused by unbalanced phase impedances is of negative sequence [9]. The above methods are not capable of decoupling the positive and negative sequence from the selective order harmonics. Therefore, when dealing with the isolated negative sequence harmonics, the order of the controller will be higher than needed, and there will be redundant parameters to be tuned.

This article, therefore, focuses on improving the harmonics suppression performance of conventional ADRC. The complex coefficient filter (CCF), which is capable of extracting orthogonal signals with selective frequency and selective phase sequence, is incorporated into the ESO so as to enhance its estimation accuracy on the d-q-axis harmonic disturbances. With the harmonic disturbances accurately estimated, the subsequently designed CCF-ADRC can achieve enhanced performance in rejecting such disturbances, while the complexity of parameter adjustment is slightly increased. The main advantages of the proposed method are summarized follows.

1) The positive and negative sequences of disturbances, caused by inverter nonlinearities and unbalanced phase impedance, are decoupled, and, respectively, suppressed.
2) The proposed CCF-ADRC inherits the advantages of conventional ADRC, such as good transient performance and parameter robustness.
3) The proposed CCF-ADRC has simpler structure and reduced order in suppressing negative sequence disturbances comparing to existing methods.

The remainder of this article is organized as follows. Section II analyzes the existing problems of conventional ADRC. Section III proposes the CCF-ESO and CCF-ADRC. Section IV presents comprehensive analysis of the proposed method. Section V verifies the effectiveness of the proposed method through experiments.

II. Problem Formulation

A. Modeling of IPMSM

Considering the influence of parameter mismatches and harmonic disturbances, the state equations of IPMSM can be modeled as

$$\begin{cases} \frac{di_d}{dt} = \frac{-R_s}{L_d} i_d + \frac{\omega_e L_q}{L_d} i_q + \frac{u_d}{L_d} + \frac{d_{\text{ddc}}+d_{\text{dac}}}{L_d} \\ \frac{di_q}{dt} = \frac{-R_s}{L_q} i_q - \frac{\omega_e L_d}{L_q} i_d - \frac{\omega_e \psi_f}{L_q} + \frac{u_q}{L_q} + \frac{d_{\text{qdc}}+d_{\text{qac}}}{L_q} \end{cases} \tag{1}$$

where R_s is the stator resistance; L_d and $L_q$are the d-axis inductance and q-axis inductance, respectively; ψ_f is the flux linkage of the permanent magnet; d_{ddc} and d_{qdc} are the aperiodic disturbances caused by parameter mismatches and voltage error between the reference voltage and actual voltage, respectively; and d_{dac} and d_{qac} are the harmonic disturbances caused by inverter nonlinearities and unbalanced phase impedances, respectively.

Then, (1) can be rewritten as

$$\begin{aligned} di_d/dt &= f_d + b_d u_d^* \\ di_q/dt &= f_q + b_q u_q^* \\ b_d &= 1/L_d \\ b_q &= 1/L_q \end{aligned} \tag{2}$$

where b_d and b_q represent control gain of d-axis and q-axis ADRC, respectively. f_d and f_q represent the total disturbances of d-axis and q-axis, which are composed of known disturbances f_0 and unknown disturbances f_1

$$\begin{cases} f_d = f_{0d} + f_{1d} \\ f_{0d} = -R_s b_d i_d + \omega_e b_d i_q / b_q \\ f_{1d} = (d_{\text{ddc}} + d_{\text{dac}})\, b_d \end{cases} \tag{3}$$

$$\begin{cases} f_q = f_{0q} + f_{1q} \\ f_{0q} = -R_s b_q i_q - \omega_e b_q \left(i_d/b_d + \psi_f\right) \\ f_{1q} = (d_{\text{qdc}} + d_{\text{qac}})\, b_q. \end{cases} \tag{4}$$

Selecting d-q-axis current i_d and i_q as the state variable x_1, expanding the unknown disturbance f_{1d} and f_{1q} into the state variable x_2, and taking the reference voltage value as the control variable u^*, the state equation becomes

$$\begin{cases} \dot{x}_{1d} = b_d u_d^* + x_{2d} + f_{0d} \\ \dot{x}_{1q} = b_q u_q^* + x_{2q} + f_{0q}. \end{cases} \tag{5}$$

B. Design of ESO

In order to estimate the unknown disturbances, ESO is constructed for the system expressed by (5), and can be written in the form of

$$\begin{cases} e_{1d} = z_{1d} - x_{1d} \\ \dot{z}_{1d} = z_{2d} - \beta_1 e_{1d} + f_{0d} + \hat{b}_d u_d^* \\ \dot{z}_{2d} = -\beta_2 e_{1d} \end{cases} \tag{6}$$

where z_{1d} is the estimated value of i_d; z_{2d} is the estimated value of unknown disturbance f_{1d}; e_{1d} is the estimated error; $\hat{b}_d$ is the estimated value of b_d; and β_1 and β_2 are the gain of ESO.

For convenience of parameter tuning and theoretical analysis, the "bandwidth" method proposed in [25] is adopted in this

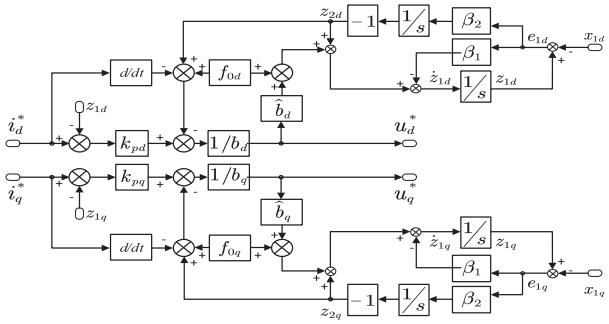

Fig. 1. Block diagram of the conventional ADRC.

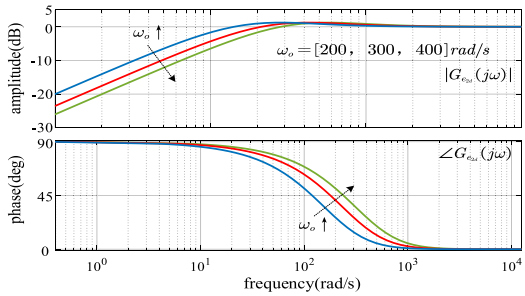

Fig. 2. Bode plot of $G_{e2d}(s)$ for $\omega_o = \{200, 300, 400\}$ (rad/s).

article, i.e.,

$$\beta_1 = 2\omega_o, \beta_2 = {\omega_o}^2. \tag{7}$$

Thus, the issue of parameter tuning is reduced to the adjustment of the observer's bandwidth "ω_o." In this way, the ESO is linearized to be LESO.

Similarly, The ESO of q-axis is shown as follows:

$$\begin{cases} e_{1q} = z_{1q} - x_{1q} \\ \dot{z}_{1q} = z_{2q} - \beta_1 e_{1q} + f_{0q} + \hat{b}_q u_q^* \\ \dot{z}_{2q} = -\beta_2 e_{1q} \end{cases} \tag{8}$$

where z_{1q} is the estimated value of i_q; z_{2q} is the estimated value of unknown disturbance f_{1q}; e_{1q} is the estimated error; and $\hat{b}_q$ is the estimated value of b_q.

C. Design of ADRC's Control Law

Defining the reference of d-axis stator current as ${i_d}^*$, the tracking error of d-axis stator current can be expressed as $e_{2d} = {i_d}^* - i_d$, then

$$\dot{e}_{2d} = \dot{{i}}_d^* - \dot{x}_1 = \dot{{i}}_d^* - \hat{b}_d {u_d}^* - \hat{f}_{0d} - x_{2d}. \tag{9}$$

The linear proportional feedback control law is adopted

$$\dot{e}_{2d} = -k_{pd} e_{2d} \tag{10}$$

where k_{pd} is the proportional gain of d-axis ADRC. Besides, instead of x_1, z_1 is used as feedback to reduce the impact of measurement noise on the system. Therefore, the d-axis control quantity can be obtained

$${u_d}^* = \frac{\dot{{i}}_d^* + k_{pd}\left({i_d}^* - z_{1d}\right) - \left(z_{2d} + \hat{f}_{0d}\right)}{\hat{b}_d}. \tag{11}$$

Similarly, the control quantity of q-axis ADRC can be obtained

$${u_q}^* = \frac{\dot{{i}}_q^* + k_{pq}\left({i_q}^* - z_{1q}\right) - \left(z_{2q} + \hat{f}_{0q}\right)}{\hat{b}_q} \tag{12}$$

where k_{pq} is the proportional coefficient of q-axis ADRC.

Finally, the structure of conventional ADRC is shown in Fig. 1.

D. Analysis of ESO

From (6), the transfer function of disturbances estimation is given as

$$G_{2d}(s) = \frac{Z_{2d}(s)}{X_{2d}(s)} = \frac{{\omega_o}^2}{s^2 + 2\omega_o s + {\omega_o}^2} \tag{13}$$

where $Z_{2d}(s)$ and $X_{2d}(s)$ are, respectively, the Laplace transform of z_{2d} and x_{2d}. In the following, a lowercase letter is used to represent a time-domain signal, whereas the corresponding capital letter is used to describe the signal in the frequency domain, e.g., $y(t)$ and $Y(s)$.

Assuming that the disturbance is a harmonic disturbance, the expression is $A\sin(\omega_h t)$. Then the amplitude error and phase angle error of the output depends on the amplitude-frequency and phase-frequency characteristics of the transfer function, i.e.,

$$\begin{aligned} |G_{2d}(j\omega)| &= A\frac{{\omega_o}^2}{{\omega_o}^2 + {\omega_h}^2} \\ \varphi_{2d}(j\omega) &= -\arctan\left(\frac{2\omega_o\omega_h}{{\omega_o}^2 - {\omega_h}^2}\right) \end{aligned} \tag{14}$$

where ω_h is the frequency of the sinusoidal disturbance. From (14), it should be noticed that the conventional ESO can observe sinusoidal disturbances without loss of amplitude and phase when $\omega_0 >> \omega_h$. However, if the $\omega_0 \approx \omega_h$ or $\omega_0 < \omega_h$, conventional ESO will have severe amplitude attenuation and phase lag.

Based on (13), the transfer function of disturbance estimation error becomes

$$G_{e2d}(s) = \frac{Z_{2d}(s) - X_{2d}(s)}{X_{2d}(s)} = -\frac{s(s + 2\omega_o)}{(s + \omega_o)^2}. \tag{15}$$

The bode plot of $G_{e2d}(s)$ is shown in Fig. 2. It can be found that a higher bandwidth can help to reduce the estimation error, but the observer's sensitivity to noise would be increased, which is not acceptable. Consequently, the conventional ESO can only estimate the disturbance well within ESO's bandwidth.

III. Proposed Current Harmonics Suppression Method

A. Design of CCF-ESO

The CCF-ESO is developed from the previous ESO, which not only inherits the advantages of conventional ESO, such as high robustness, good transient performance, and simple parameter

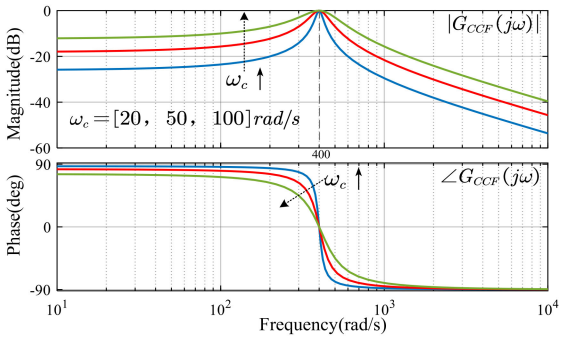

Fig. 3. Bode plot of CCF for $\omega_c = [20, 50, 100]$ rad/s.

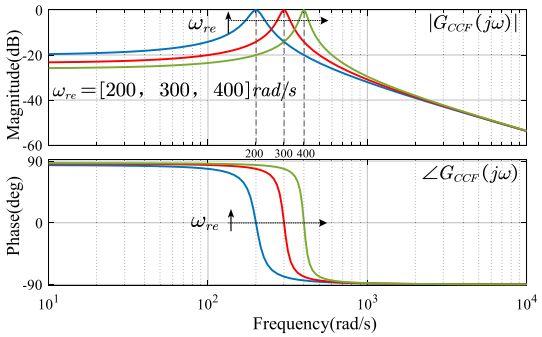

Fig. 4. Bode plot of CCF for $\omega_{re} = [200, 300, 400]$ rad/s.

tuning but also enhances the ability to deal with harmonic disturbances.

In order to accurately estimate the harmonic disturbances caused by inverter nonlinearities and unbalanced phase impedances, a CCF is introduced as

$$G_{\mathrm{CCF}}(s) = \frac{\omega_c}{s - j\omega_{re} + \omega_c} \tag{16}$$

where ω_{re} is the resonant frequency of CCF and ω_c is the cutoff frequency of CCF.

The bode plots of CCF are shown in Figs. 3 and 4. From Fig. 3, it can be found that a smaller ω_c leads to better harmonic attenuation. However, a smaller ω_c will deteriorate dynamic response. Therefore, a tradeoff between the dynamic response and harmonic attenuation is usually made in the design of CCF.

It can be seen from Fig. 4 that the CCF can extract the specified frequency (ω_{re}) component with unity gain and zero phase shift, while at the other frequencies, the amplitude will decrease. Then, the CCF-ESO of d-axis in frequency-domain is shown as follows:

$$\begin{cases} E_{1d}(s) = Z_{1d}(s) - X_{1d}(s) \\ Z_{1d}(s) = \frac{1}{s}\left[Z_{2d}(s) - \beta_1 E_{1d}(s) + F_{0d} + \hat{b}_d U_d^*(s)\right] \\ Z_{2d}(s) = -\left(G_{CCF}(s) + \frac{1}{s}\right)\beta_2 E_{1d}(s). \end{cases} \tag{17}$$

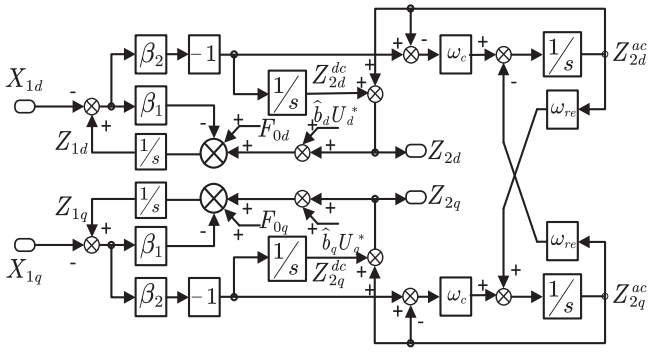

Fig. 5. Block diagram of the CCF-ESO.

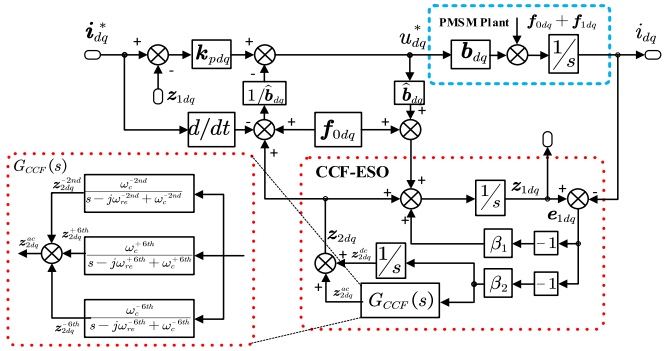

Fig. 6. Block diagram of the CCF-ADRC.

Similarly, The CCF-ESO of q-axis in frequency domain is shown as follows:

$$\begin{cases} E_{1q}(s) = Z_{1q}(s) - X_{1q}(s) \\ Z_{1q}(s) = \frac{1}{s}\left[Z_2(s) - \beta_1 E_{1q}(s) + F_{0q} + \hat{b}_q U_q^*(s)\right] \\ Z_{2q}(s) = -\left(G_{\mathrm{CCF}}(s) + \frac{1}{s}\right)\beta_2 E_{1q}(s). \end{cases} \tag{18}$$

Compared with the conventional ESO, the CCF-ESO inserts a CCF in the second order to extract harmonic disturbances. Obviously, $Z_{2d}(s)$and $Z_{2q}(s)$ can be decomposed as follows:

$$\begin{cases} Z_{2d}(s) = Z_{2d}^{dc}(s) + Z_{2d}^{ac}(s) \\ Z_{2q}(s) = Z_{2q}^{dc}(s) + Z_{2q}^{ac}(s) \end{cases} \tag{19}$$

where $Z_{2d(q)}^{dc}(s)$ and $Z_{2d(q)}^{ac}(s)$ represent the estimated value of aperiodic disturbances and harmonic disturbances, respectively. The block diagram of CCF-ESO is shown in Fig. 5.

B. Design of CCF-ADRC Considering Inverter Nonlinearities and Unbalanced Phase Impedance

Replace the conventional ESO of ADRC with CCF-ADRC to obtain CCF-ADRC.

In order to accurately estimate and suppress the disturbances caused by the nonlinearities of the inverter ($\pm$6th) and unbalanced phase impedances ($-$2nd), the resonant frequency of CCF-ESO needs to be set to as

$$\omega_{re}^{\pm 6th} = \pm 6\omega_{re}, \omega_{re}^{-2nd} = -2\omega_{re}. \tag{20}$$

Then, the structure of the CCF-ADRC can be obtained, as shown in Fig. 6. It should be noticed that the negative

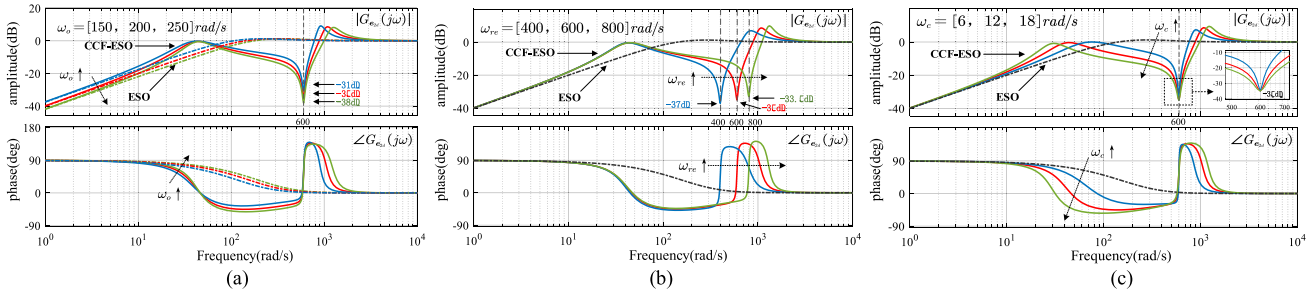

Fig. 7. Bode plot of $G_{e2d}(s)$ under different parameters. (a) $\omega_o = \{150, 200, 250\}$ (rad/s) (b) $\omega_{re} = \{400, 600, 800\}$ (rad/s). (c) $\omega_c = \{6, 12, 18\}$ (rad/s).

sequence harmonic disturbances caused by unbalanced phase impedances is -second-order [9], while the phase sequence of harmonic disturbances caused by inverter nonlinearities have positive sequence (+sixth) and negative sequence (-sixth) harmonics. In fact, CCF-ESO is a bit similar to GI-ESO proposed in [28], GI-ESO can also effectively deal with such selective order harmonic disturbances. However, it cannot decouple the positive sequence and the negative sequence. Therefore, when dealing with isolated negative sequence disturbances caused by unbalanced phase impedance, the order of GI-ESO is higher than needed, hence the structure is more complicated than the CCF-ESO.

IV. Analysis of CCF-ESO and CCF-ADRC

A. Harmonics Estimation Capability of CCF-ESO

In order to show the superiority of CCF-ESO in estimating harmonic disturbances, the transfer function between z_{2d} and x_{2d} of CCF-ESO can be obtained

$$G_{2d}(s) = \frac{(\beta_2 + \beta_2\omega_c)\, s + \beta_2\omega_c - \beta_2\omega_{re} j}{\lambda(s)}. \tag{21}$$

Similarly, the transfer function of disturbances estimation error becomes

$$G_{e2d}(s) = \frac{s\,(\beta_1 + s)\;(\omega_c + s - \omega_0 j)}{\lambda(s)} \tag{22}$$

where $\lambda(s)$ is the characteristic polynomial, and the expression of $\lambda(s)$ is

$$\begin{aligned}\lambda(s) = {} & s^3 + (\beta_1 + \omega_c - j\omega_{re})\, s^2 \\ & + (\beta_2 + (\beta_1 + \beta_2)\,\omega_c - j\beta_1\omega_{re})\, s \\ & + \beta_2\omega_c - j\beta_2\omega_{re}.\end{aligned} \tag{23}$$

Substituting (7) into (23), then $\lambda(s)$ can be derived as

$$\begin{aligned}\lambda(s) = {} & s^3 + (2\omega_o + \omega_c - j\omega_{re})\, s^2 \\ & + \left(\omega_o^2 + (2\omega_o + \omega_o^2)\,\omega_c - j2\omega_o\omega_{re}\right) s \\ & + \omega_o^2\omega_c - j\omega_o^2\omega_{re}.\end{aligned} \tag{24}$$

The bode plots of $G_{e2d}(s)$ for different ω_o, ω_{re}, and ω_c are shown in Fig. 7. It is noteworthy that CCF-ESO and ESO have similar frequency characteristics at very low and high-frequency range. Moreover, the bode plots show the superiority of CCF-ESO in dealing with harmonic disturbances. The reason is that the inserted CCF enable rather high gains at specific resonant frequency.

TABLE I
Generalized Routh Array for Complex Coefficient Polynomial

s^3	a_0	b_1	a_2	b_3
s^2	a_1	b_2	a_3	
	$b_1^{(1)}$	$a_2^{(1)}$	$b_3^{(1)}$	
s^1	$a_2^{(2)}$	$b_3^{(2)}$		
	$b_2^{(1)}$	$a_3^{(1)}$		
s^0	$a_3^{(2)}$			
	$b_3^{(3)}$			

B. Stability Analysis of CCF-ESO

The stability of CCF-ESO can be evaluated by analyzing the root distribution of the characteristic polynomial described in (24). Since the characteristic polynomial $\lambda(s)$ is a complex coefficient characteristic polynomial, the conventional Routh criterion cannot be directly adopted. Therefore, the generalized Routh criterion proposed in [33] is introduced in this article. According to [33], for a third-order complex coefficient characteristic equation described in (25), the generalized Routh array is given in Table I

$$F(s) = s^3 + (a_1 + jb_1)\, s^2 + (a_2 + jb_2)\, s + (a_3 + jb_3) \tag{25}$$

where

$$\begin{aligned}a_0 &= 1,\ a_1 = 2\omega_o + \omega_c,\ b_1 = -\omega_{re},\ a_2 \\ &= \omega_o^2 + \left(2\omega_o + \omega_o^2\right)\omega_c, \\ b_2 &= -2\omega_o\omega_{re},\ a_3 = \omega_o^2\omega_c,\ b_3 = -\omega_o^2\omega_{re} \\ a_2^{(2)} &= 4\,(\omega_c + 1)\,\omega_o^4 + 2\,(2\omega_c + 5)\,\omega_c\omega_o^3 \\ &\quad + (\omega_c + 8)\,\omega_c^2\omega_o^2 + 2\left(\omega_c^2 + \omega_{re}^2\right)\omega_c\omega_o \\ a_3^{(2)} &= \omega_o^4\omega_c(2\omega_o + \omega_c)^2 \\ &\quad \times \begin{pmatrix} 4(\omega_c + 1)^2\omega_o^4 + 4\left(\omega_c^3 + 5\omega_c^2 + 4\omega_c + 2\omega_{re}^2\right)\omega_o^3 \\ + \left(\omega_c^4 + 16\omega_c^3 + 24\omega_c^2 + 8\omega_c\omega_{re}^2\right)\omega_o^2 \\ + 4\omega_c\,(\omega_c + 4)\left(\omega_c^2 + \omega_{re}^2\right)\omega_o + 4\left(\omega_c^2 + \omega_{re}^2\right)^2 \end{pmatrix}.\end{aligned}$$

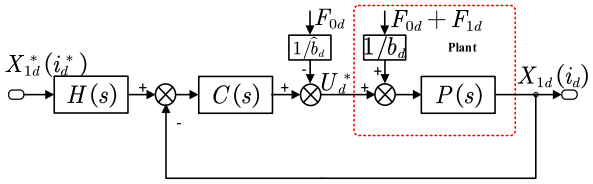

Fig. 8. Two-degree-of-freedom equivalent model of CCF-ADRC.

The stability condition for the third-order complex coefficient characteristic equation is given as

$$a_0 > 0, a_1 > 0, {a_2}^{(2)} > 0, {a_3}^{(2)} > 0. \tag{26}$$

Obviously, in (24), ω_c, ω_0, and ω_{re}^2 are both positive. Then, ${a_2}^{(2)}$ and ${a_3}^{(2)}$ are positive. Therefore, CCF-ESO is stable.

C. Harmonics Rejection Capability of CCF-ADRC

To analyze the stability of the entire closed-loop system, the d-axis CCF-ADRC is simplified into a standard two-degree-of-freedom controller as shown in the Fig. 8. X_{1d}^* represents the command input; X_{1d} represents the system output; $H(s)$ represents the command filtering part; $C(s)$represents the controller part; $P(s)$ represents the controlled plant; and F_{0d} and F_{1d} represent the known and unknown disturbances. Besides, to simplify the analysis, it is assumed that the estimated value of control gain is accurate, i.e., $\hat{b}_d = b_d$.

Transfer the d-axis CCF-ADRC control law (11) into frequency domain

$$\hat{b}_d U_d^*(s) = s i_d^* + k_{pd}\left(i_d^* - Z_{1d}(s)\right) - \left(Z_{2d}(s) + F_{0d}(s)\right). \tag{27}$$

Substituting d-axis CCF-ESO (17) into (27), then (27) can be rewritten as

$$U_d^*(s) = L_1(s) X_{1d}(s) + L_2(s) i_d^* - F_{0d}(s)/\hat{b}_d \tag{28}$$

where

$$L_1(s) = -\frac{G_{\mathrm{CCF}}(s){\omega_o}^2 s^2 + \left(G_{\mathrm{CCF}}(s) k_{pd} {\omega_o}^2 + 2k_{pd}\omega_o + {\omega_o}^2\right)s + k_{pd}{\omega_o}^2}{\hat{b}_d s(k_{pd} + 2\omega_o + s)}$$

$$L_2(s) = \frac{(s + k_{pd})\left(s^2 + \left(G_{\mathrm{CCF}}{\omega_o}^2 + 2\omega_o\right)s + {\omega_o}^2\right)}{\hat{b}_d s\left(k_{pd} + 2\omega_o + s\right)}.$$

Then, the transfer functions of $P(s)$, $C(s)$, and $H(s)$are deduced as follows:

$$\begin{cases} P(s) = \frac{b_d}{s} \\ C(s) = -L_1(s) \\ \quad = \frac{G_{\mathrm{CCF}}(s){\omega_o}^2 s^2 + \left(G_{\mathrm{CCF}}(s) k_{pd} {\omega_o}^2 + 2k_{pd}\omega_o + {\omega_o}^2\right)s + k_{pd}{\omega_o}^2}{\hat{b}_d s(k_{pd} + 2\omega_o + s)} \\ H(s) = \frac{-L_2(s)}{L_1(s)} \\ \quad = \frac{(s + k_{pd})\left(s^2 + \left(G_{\mathrm{CCF}}{\omega_o}^2 + 2\omega_o\right)s + {\omega_o}^2\right)}{G_{\mathrm{CCF}}(s){\omega_o}^2 s^2 + \left(G_{\mathrm{CCF}}(s) k_{pd} {\omega_o}^2 + 2k_{pd}\omega_o + {\omega_o}^2\right)s + k_{pd}{\omega_o}^2}. \end{cases} \tag{29}$$

Assuming that the command input X_{1d}^* is zero, the transfer function of d-axis CCF-ADRC between the system output X_{1d} and the unknown disturbances F_{1d} can be expressed as (30) shown at the bottom of this page.

Fig. 9 shows the bode plots of $G_{F_{1d}}(s)$ under different ω_{re}, ω_o, and k_{pd}. The curves for the CCF-ADRC and for the conventional ADRC are in solid line and dashed line, respectively. It can be seen from Fig. 9(a) that the frequency characteristics of CCF-ADRC and conventional ADRC have a small difference in low- and high-frequency bands. However, CCF-ADRC has a significant amplitude attenuation suppresses harmonic disturbances at the resonant frequency. It can also be seen from Fig. 9(b) that as the bandwidth increases, the amplitude of CCF-ADRC and ADRC has a considerable decrease in the low frequency, which means that the low frequency disturbances rejection capability is enhanced. Besides, it can be found that the change of ω_0 or k_{pd} does not affect the disturbances rejection capability of CCF-ADRC at the resonant frequency.

To verify the negative sequence harmonic disturbance rejection performance of CCF-ADRC, the bode plot in full frequency domain considering the inverter nonlinearities and unbalanced phase impedances is shown in Fig. 10. It can be found that the CCF-ADRC can suppress the isolated negative sequence harmonic disturbances (second) caused by unbalanced phase impedances.

D. Command Tracking Performance of CCF-ADRC

Assuming that the unknown disturbances F_{1d} is zero, then the transfer function between the system output X_{1d} and the input command X_{1d}^* can be obtained as

$$G_R(s) = \frac{i_d(s)}{i_d^*(s)} = \frac{X_{1d}(s)}{X_{1d}^*(s)} = \frac{H(s) C(s) P(s)}{1 + C(s) P(s)} = 1. \tag{31}$$

It is obvious from (31) that the system output X_{1d} can fully track the input command X_{1d}^*. Hence, when CCF-ADRC enhances the harmonic disturbances rejection capability, it will not affect its tracking performance. Consequently, CCF-ADRC still retains a major advantage of the conventional ADRC, namely, tracking performance and harmonics rejection performance completely decoupled.

It should be emphasized that the result of (31) is just an ideal result. In practice, it is impossible to be completely equal to unity, due to the following reasons.

1) The ideal differential operation of the control law cannot be realized. The noise in the practical system cannot be avoided. In order to suppress the noise, a phase lag during the differential process is inevitable.
2) The model parameters of ADRC should be completely accurate. However, if there exist inductance mismatches or resistance mismatches, the results of (31) will not equal

$$\begin{aligned} G_{F_{1d}}(s) &= \frac{i_d(s)}{F_{1d}(s)} = \frac{X_{1d}(s)}{X_{2d}(s)} = \frac{P(s)/b_d}{1 + C(s)P(s)} \\ &= \frac{s(s + k_{pd} + 2\omega_o)}{s^3 + \left[G_{CCF}(s){\omega_o}^2 + 2\omega_o + k_{pd}\right]s^2 + \left[G_{CCF}(s) k_{pd}{\omega_o}^2 + 2k_{pd}\omega_o + {\omega_o}^2\right]s + k_{pd}{\omega_o}^2}. \end{aligned} \tag{30}$$

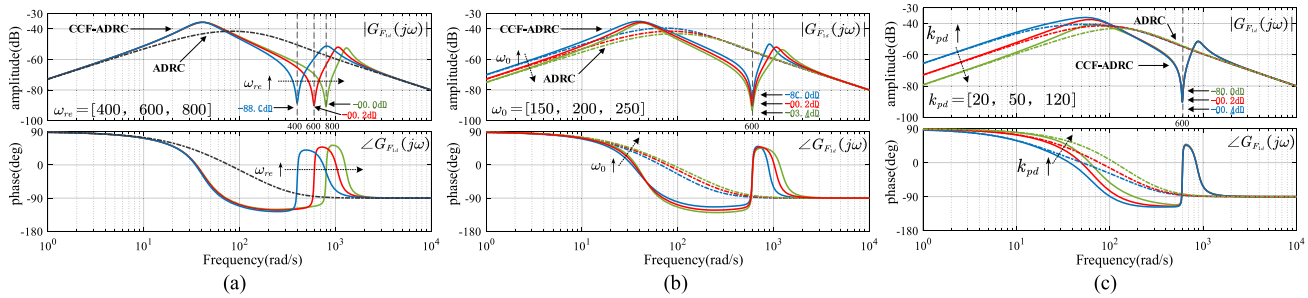

Fig. 9. Bode plot of $G_{F1d}(s)$ under different parameters. (a) $\omega_c = 0.02\omega_{re}, \omega_0 = 200, k_{pd} = 50, \omega_{re} = \{400, 600, 800\}$. (b) $\omega_c = 0.02\omega_{re}, \omega_{re} = 600, k_{pd} = 50, \omega_0 = \{150, 200, 250\}$. (c) $\omega_c = 0.02\omega_{re}, \omega_{re} = 600, \omega_0 = 200, k_{pd} = \{20, 50, 120\}$.

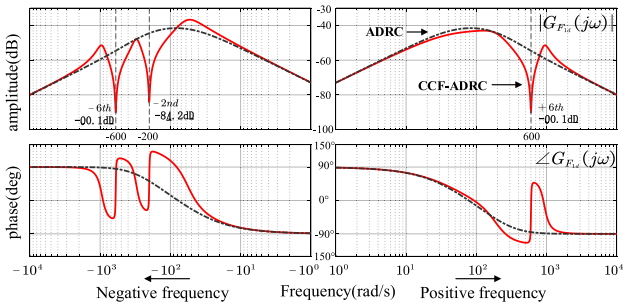

Fig. 10. Bode plot of $G_{F1d}(s)$ in positive and negative frequency domain.

to unity. The effect of inductance mismatches will be analyzed in the next section.

3) The estimation result of the unknown disturbances should be completely accurate. However, many nonideal factors in the practical system, such as sampling error, model nonlinearity, and control delay, will make the modeling and observation of disturbance inaccurate.

E. Parameter Robustness Analysis

The control gain is a very important parameter for ADRC. Therefore, it is necessary to analyze the effect of control gains mismatch on the performance of CCF-ADRC.

According to (17), the transfer function of *d*-axis CCF-ESO can be expressed as

$$\begin{aligned} Z_{1d}(s) &= \frac{\beta_1 s^2 + (\beta_1\omega_c + \beta_2\omega_c + \beta_2 - \beta_1\omega_{re}j)\, s}{\lambda(s)} X_{1d}(s) \\ &\quad + \frac{\beta_2\omega_c - \beta_2\omega_{re}j}{\lambda(s)} X_{1d}(s) + \frac{\hat{b}_d s^2 + (\hat{b}_d\omega_c - \hat{b}_d\omega_{re}j)s}{\lambda(s)} U_d^* \\ &\quad + \frac{s^2 + (\omega_c - \omega_{re}j)\, s}{\lambda(s)} F_{0d}(s) \\ Z_{2d}(s) &= \frac{\beta_2 s\left((1+\omega_c)\, s + \omega_c - \omega_{re}j\right)}{\lambda(s)} X_{1d}(s) \\ &\quad - \frac{\hat{b}_d\beta_2\left((1+\omega_c)\, s + \omega_c - \omega_{re}j\right)}{\lambda(s)} U_d^* \\ &\quad - \frac{\beta_2\left((1+\omega_c)\, s + \omega_c - \omega_{re}j\right)}{\lambda(s)} F_{0d}(s). \end{aligned} \tag{32}$$

Substitute (32) into (27)

$$\hat{b}_d U_d^* = \frac{(s+k_{pd})\, j\lambda(s)}{sG_1(s)} i_d^* - \frac{jG_2(s)}{sG_1(s)} X_{1d}(s) - F_{0d}(s) \tag{33}$$

where

$$\begin{aligned} G_1(s) &= (s + \beta_1 + k_{pd})(sj + \omega_c j + \omega_{re}) \\ G_2(s) &= (\beta_2 + \beta_2\omega_c + \beta_1 k_{pd})\, s^2 \\ &\quad + (\beta_2 k_{pd} + \beta_2\omega_c + \beta_1 k_{pd}\omega_c + \beta_2 k_{pd}\omega_c \\ &\quad - \beta_2\omega_{re}j - \beta_1 k_{pd}\omega_{re}j)s + \beta_2 k_{pd}\omega_c - \beta_2 k_{pd}\omega_{re}j. \end{aligned}$$

Substitute (32) into (33)

$$\begin{aligned} &\frac{\hat{b}_d}{b_d}\left(sX_{1d}(s) - F_{0d}(s) - X_{2d}(s)\right) \\ &\quad = \frac{(s+k_{pd})\, j\lambda(s)}{sG_1(s)} i_d^* - \frac{jG_2(s)}{sG_1(s)} X_{1d}(s) - F_{0d}(s). \end{aligned} \tag{34}$$

Defining control gain ratio $r_b = \hat{b}_d/b_d$, then (34) can be rewritten as

$$\begin{aligned} X_{1d}(s) &= \frac{(s+k_{pd})j\lambda(s)}{r_b s^2 G_1(s) + jG_2(s)} i_d^* + \frac{r_b s G_1(s)}{r_b s^2 G_1(s) + jG_2(s)} X_{2d} \\ &\quad + \frac{sG_1(s)}{r_b s^2 G_1(s) + jG_2(s)}\left(r_b F_{0d} - F_{0d}(s)\right). \end{aligned} \tag{35}$$

Defining the characteristic polynomial $R(s)$ of CCF-ADRC is

$$R(s) = r_b s^2 G_1(s) + jG_2(s). \tag{36}$$

It can be seen from (36) that the control gain r_b mismatches will affect the closed-loop performance of ADRC. This effect includes closed-loop stability, command tracking performance, and disturbance rejection performance.

1) Influence of r_b on Closed-Loop Stability: To analyze the influence of r_b on the closed-loop stability, the closed-loop pole distribution can be plotted by directly computing the roots of the closed-loop characteristic polynomial $R(s)$.

When r_b is changed from 0.1 to 1000, the distribution of closed-loop poles is shown in Fig. 11. As can be seen from Fig. 11, the poles of the closed-loop system are always in the left plane of s. Therefore, the system is always stable.

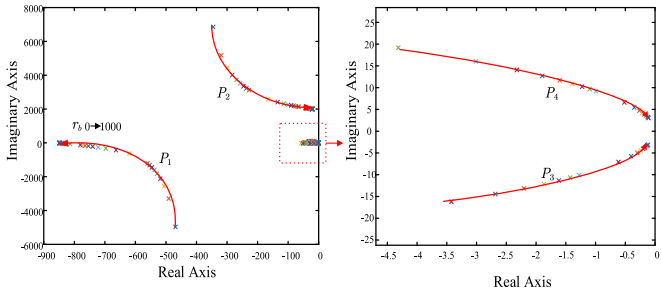

Fig. 11. Close loop pole distribution under different r_b.

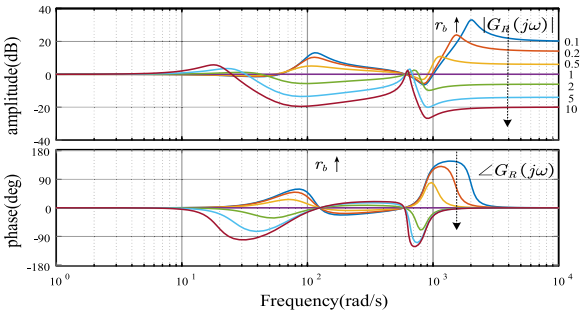

Fig. 12. Bode plot of $G_R(s)$ under different r_b.

2) Influence of r_b on Command Tracking Capability: According to (35), the transfer function between current feedback value and the current reference value is

$$G_R(s) = \frac{i_d(s)}{i_d^*(s)} = \frac{X_{1d}(s)}{X_{1d}^*(s)} = \frac{(s+k_{pd})\,j\lambda(s)}{r_b s^2 G_1(s) + jG_2(s)}. \quad (37)$$

The bode plots of $G_r(s)$ under different control gain ratios $r_b = \hat{b}_d/b_d$ are shown in Fig. 12. The bandwidth ω_o of ESO is 200 rad/s, the proportional gain k_{pd} is 50. According to Fig. 12, The following conclusions can be obtained.

1) When $r_b = 1$, the system exhibits unity gain characteristics, i.e., the system output can fully track the input command over the entire frequency band.
2) When $r_b \in (1, 10)$, The system has a fixed amplitude attenuation in the high-frequency band, and the degree of attenuation is positively correlated with r_b.
3) When $r_b \in (0.1, 1)$, The system has a fixed amplitude amplification in the high-frequency band, and the degree of amplification is positively correlated with r_b.
4) The low-frequency command tracking performance of the system is almost unaffected, which means that when tracking a low-frequency command signal, the system has a high tolerance for inaccurate control gains.
5) Influence of r_b on disturbance rejection capability

According to (35), the transfer function between current feedback value and the unknown disturbances is

$$G_{F_{1d}}(s) = \frac{i_d(s)}{F_{1d}(s)} = \frac{X_{1d}(s)}{X_{2d}(s)} = \frac{r_b s G_1(s)}{r_b s^2 G_1(s) + jG_2(s)}. \quad (38)$$

The bode plots of $G_{F_{1d}}(s)$ under different control gain ratios $r_b = \hat{b}_d/b_d$ (0.1–10) are shown in Fig. 13. The bandwidth ω_o of

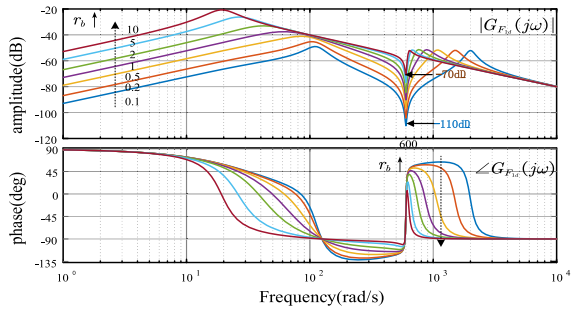

Fig. 13. Bode plot of $G_{F_{1d}}(s)$ under different r_b.

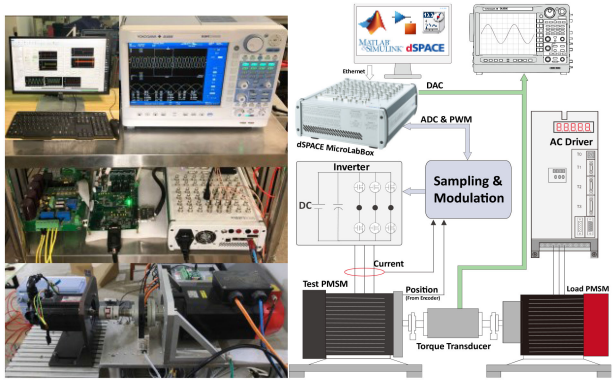

Fig. 14. (a) Experimental platform. (b) Block diagram of the platform.

ESO is 200 rad/s, the proportional gain k_{pd} is 50. According to Fig. 13, the following conclusions can be obtained.

1) r_b is smaller, the disturbances rejection performance in the low- and middle-frequency bands is stronger.
2) For low-frequency unknown disturbance, the gain can be kept below -40 dB.
3) For unknown disturbance at the resonant frequency, the disturbances rejection performance of CCF-ADRC is stronger than ADRC. Besides, the attenuation peak of CCF-ADRC at the resonant frequency decreases with the increase of control gain ratio, but the change is not obvious (from -70 to -110 dB). Therefore, the disturbances rejection performance has highly tolerant to the control gain mismatches.

V. Experimental Results

In this section, the experimental results of the proposed and the conventional ADRC scheme are presented and compared. Fig. 14 shows the experiment platform for the IPMSM drive system. The conventional ADRC and proposed CCF-ADRC are implemented on a dSPACE MicroLabBox real-time platform with ControlDesk and Matlab, respectively. The dSPACE controller is connected to the VSI through a modulation board. The pulse width modulation (PWM) switching frequency is set to 5 kHz. The dc-link voltage is set to 240 V. The parameters for conventional ESO and CCF-ESO are set to $\beta_1 = 800$ and $\beta_2 = 160\,000$ to achieve a bandwidth of 400 rad/s. In addition,

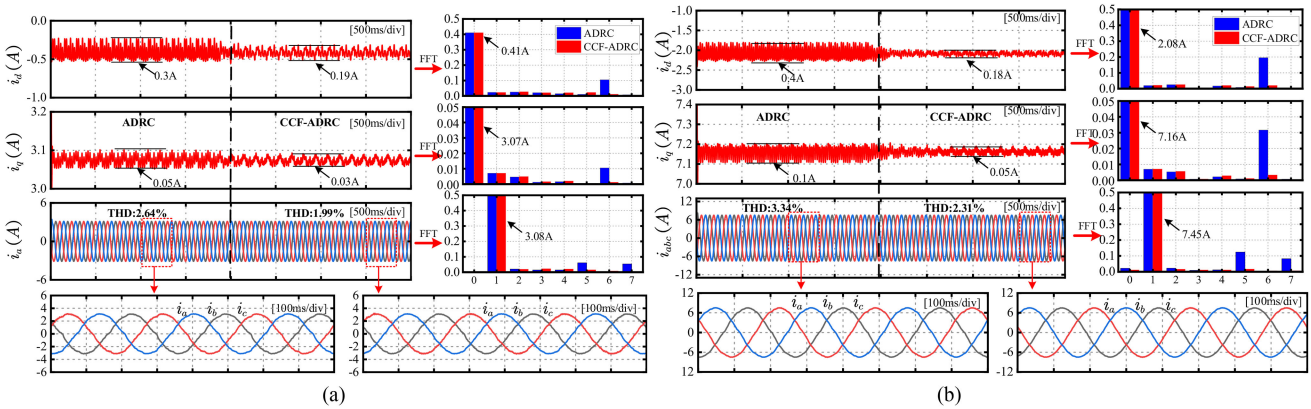

Fig. 15. Experimental results of *d*-*q*-axis and phase current waveforms and FFT results at 150 r/min. (a) Under light load. (b) Under rated load.

TABLE II
IPMSM PARAMETERS

Parameters	Symbols	Values
Stator Resistance	R_s	0.75 Ω
Stator d-axis Inductance	L_d	3.5 mH
Stator q-axis Inductance	L_q	9.8 mH
Rotor Flux Linkage	ψ_f	0.142 Wb
Rated Power	P_n	1.0 kW
Rated Torque	T_{en}	5 N·m
Rated frequency	f_n	75 Hz
Number of Pole Pairs	N_p	3

the conventional ADRC and the proposed CCF-ADRC are with the same proportional coefficient, i.e., $k_{pd} = k_{pq} = 30$. The parameters of the test motor are listed in Table II.

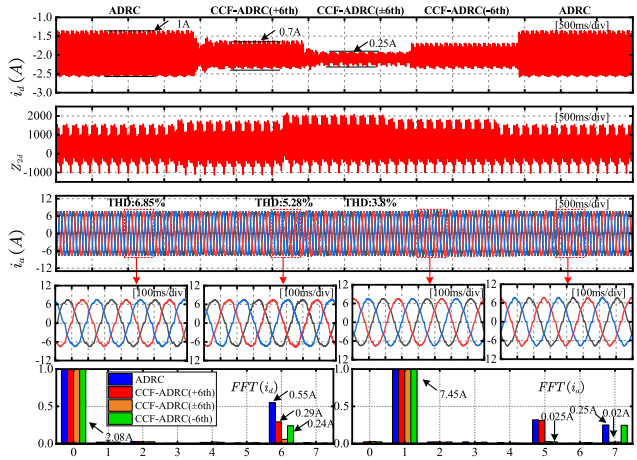

Fig. 16. Experimental results of *d*-axis and phase current and *d*-axis harmonic disturbance waveforms and FFT results at 150 r/min under rated load.

A. *Steady-State Experiment*

To verify the harmonic disturbances suppression capability of CCF-ADRC, the steady-state experiment separately analyzed three situations, where only inverter nonlinearities, unbalanced phase impedance, and inverter nonlinearities and unbalanced phase impedance are considered simultaneously.

1) Experimental Results Considering Inverter Nonlinearities: In the first experiment, the deadtime is set to 5 us to highlight the experimental phenomenon of inverter nonlinearities. The parameters are set to $\omega_{re}^{\pm 6th} = \pm 6\omega_e$ and $\omega_c^{\pm 6th} = 0.0005\omega_e$ for CCF-ESO. Fig. 15 shows the waveform when the motor is operated at 150 r/min under the light load (2 N·m) and rated load (5 N·m) conditions, respectively. Fig. 15(a) shows the *d*-*q*-axis current, the phase current, and their fast fourier transform (FFT) results of the conventional ADRC and CCF-ADRC under the light load condition. Before the CCF-ADRC is enabled, the current ripples of *d*-axis and *q*-axis are approximately 0.3 and 0.05 A, respectively, while the THD of phase current is 2.64%. After enabling the proposed CCF-ADRC, the current ripples of *d*-axis and *q*-axis current decrease to approximately 0.19 and 0.03 A, respectively, while the THD of phase current decreases to 1.99%. Besides, the sixth-order current harmonics of *d*-axis and *q*-axis are reduced from 0.1 to 0.01 A and 0.01 to 0.001 A, respectively. The fifth and seventh-order current harmonics of phase current are reduced from 0.014 to 0.02 A and 0.002 to 0.007 A, respectively.

The effectiveness of the proposed CCF-ADRC is also evaluated under rated load shown in Fig. 15(b). Obviously, with the load torque increasing, the current distortion seriously increases. With the proposed CCF-ADRC, the current ripples of *d*-axis and *q*-axis current decrease to approximately 0.18 and 0.05 A, respectively, while the total harmonic distortion (THD) of phase current decreases to 2.31%. Besides, the sixth-order current harmonics of *d*-axis and *q*-axis are reduced from 0.196 to 0.02 A and 0.032 to 0.003 A, respectively. The sixth and seventh-order current harmonics of phase current are reduced from 0.124 to 0.016 A and 0.08 to 0.005 A, respectively.

To verify the phase sequence decoupling ability of CCF-ADRC. The resonant frequency ω_{re} is set to $+6\omega_e$, $-6\omega_e$ and $\pm 6\omega_e$. Fig. 16 shows the *d*-axis current, *d*-axis estimated disturbances z_{2d}, phase current waveforms, and FFT results of

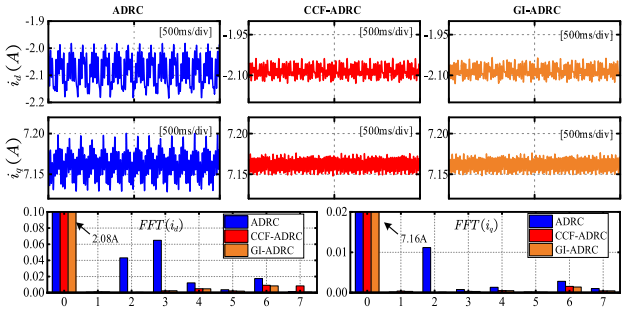

Fig. 17. Experimental results of d-q-axis and phase current waveforms and FFT results at 15 0r/min under rated load.

the conventional ADRC and CCF-ADRC under the rated load, respectively.

It is obvious that when ω_{re} is set to $+6\omega_e$, the sixth-order current harmonic of d-axis is decreased from 0.55 to 0.29 A and the seventh-order current harmonic of phase current is reduced from 0.25 to 0.02 A, while the fifth-order current harmonics almost does not change. When ω_{re} is set to $-6\omega_e$, the sixth-order current harmonic of d-axis is decreased from 0.55 to 0.24 A. and the fifth-order current harmonic of phase current is reduced from 0.32 to 0.025 A, while the seventh-order current harmonics almost does not change. However, both fifth and seventh-order harmonics of the phase current will be significantly reduced if ω_{re} is set to $\pm 6\omega_e$.

2) Experimental Results Considering Unbalanced Phase Impedances: In the second experiment, the deadtime of PWM is set to 1 us to weaken the influence of inverter nonlinearities. In addition, to highlight the experimental phenomenon of unbalanced phase impedances, a 0.15-Ωresistor and 2.1-mH inductance are connected in series between the A-phase output of the inverter and the A-phase input of the IPMSM. The parameters are set to $\omega_{re}^{-2nd} = -2\omega_e$ and $\omega_c^{-2nd} = 0.002\omega_e$ for CCF-ESO. The experimental conditions are the same as the first experiment and the experimental results are shown in Fig. 17.

Due to the unbalanced phase impedance, the -second-order harmonic appears in the i_d and i_q. Fig. 17 shows the d-axis and q-axis current and their FFT results of the conventional ADRC and CCF-ADRC under the rated load, respectively. From the FFT results, the -second-order harmonics in i_d and i_q declines from 0.043 to 0.00021 A and 0.01117 to 0.000514 A.

To illustrate the advantages of CCF-ADRC compared to GI-ADRC. The experimental results of ADRC, CCF-ADRC, and GI-ADRC simultaneously are shown in Fig. 17. Obviously, although GI-ADRC also suppresses the -second-order harmonic, its order is higher than CCF-ADRC, hence its structure is also more complicated than the CCF-ADRC.

3) Experimental Results Considering Inverter Nonlinearities and Unbalanced Phase Impedances Simultaneously: In the third experiment, the deadtime of PWM is set to 5 us and additional resistors and inductors are used to simulate the unbalanced phase impedance of the IPMSM. The experimental conditions and parameters are the same as the first and second experiments and the experimental results are shown in Fig. 18.

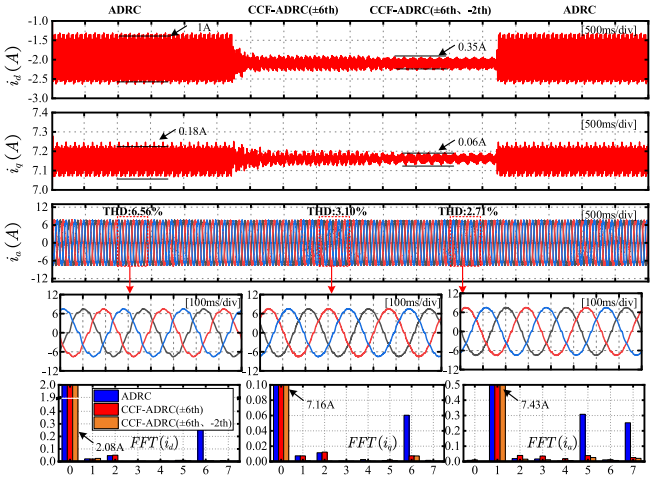

Fig. 18. Experimental results of d-q-axis and phase current waveforms and FFT results at 150 r/min under rated load.

Obviously, due to the inverter nonlinearities and the unbalanced phase impedance are existed simultaneously,the distortion of i_a, i_d, and i_q are very serious before the CCF-ADRC is enabled. After enabling the proposed CCF-ADRC, the distortion in the i_a, i_d, and i_q are very well suppressed. From the FFT results, it can be seen that second, fifth, and seventh-order harmonics in i_d and i_q are obviously reduced. The THD declines from 6.56% to 2.71%, showing the effectiveness of the proposed CCF-ADRC. Besides, in the d-axis and q-axis current waveform, the ripples decrease from 1 to 0.35 A and 0.18 to 0.06 A, respectively.

B. Experimental Results Under Mismatched Parameters

A parameter mismatches experiment is carried out to verify the robust performance of the CCF-ADRC. The resistance and inductance of d-q-axis are selected as test parameters.

Fig. 19(a) shows the experiment results of the CCF-ADRC under resistance mismatches. When the motor is running at 150-r/min under rated load and the resistance value is increased to 2 times the rated value and decreased to 0.5 times the rated value at 0.5 and 1.5 s, respectively.

Fig. 19(b) and (c) shows the experiment results of the CCF-ADRC under d-axis and q-axis inductance mismatches with the same test conditions, respectively.

From these results, it can be found that neither the resistance mismatch nor the inductance mismatch has little effect on the steady-state performance. Therefore, the CCF-ADRC retains the robustness of the conventional ADRC to parameters mismatch.

B. Experimental Results in Tracking Step Reference and Sinusoidal Reference

In this experiment, the performance of CCF-ADRC in tracking step reference and sinusoidal reference is examined. Fig. 20 shows the tracking waveform of i_q using the conventional ADRC and using the CCF-ADRC. As can be seen, the proposed CCF-ADRC still retains the good tracking performance

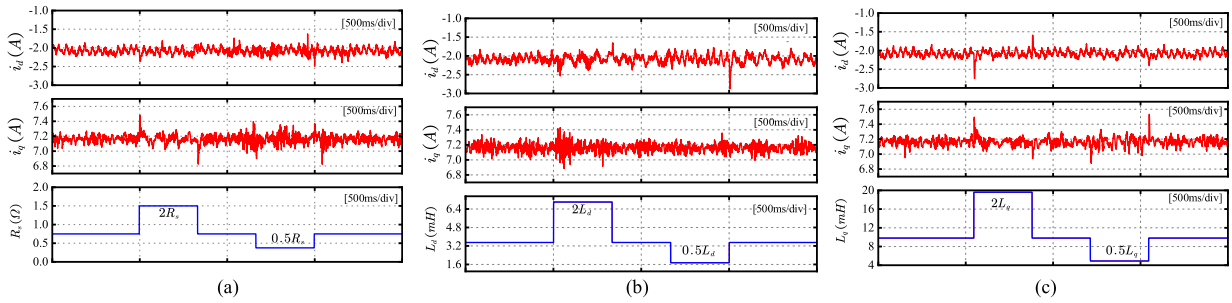

Fig. 19. Experimental results of *d*-*q*-axis current waveforms with parameters mismatches at 150 r/min under rated load. (a) Resistance mismatch. (b) *d*-axis inductance mismatch. (c) *q*-axis inductance mismatch.

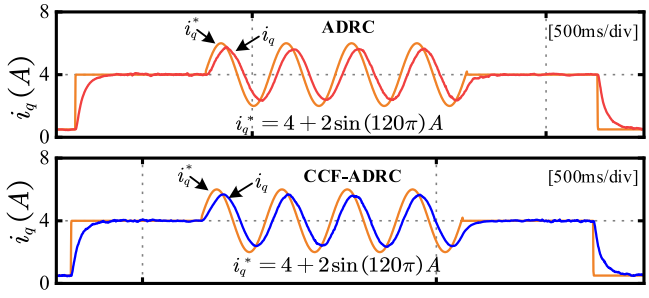

Fig. 20. Experimental results of *q*-axis current waveforms in tracking step reference and sinusoidal reference.

of conventional ADRC. Overall, the proposed method shows good performance both under steady state and under transient state.

VI. Conclusion

In this article, a novel CCF-ADRC is proposed to suppress current harmonics of IPMSM drives. The stability, the harmonics rejection performance, the command tracking performance, and the influence of parameter mismatches on the proposed method are analyzed in detail. Comparing to the conventional ADRC, the proposed CCF-ADRC has a better capability in suppressing harmonic disturbances. Comparing to the GI-ADRC, CCF-ADRC has simpler structure and reduced order in suppressing negative sequence disturbances. In the meanwhile, CCF-ADRC inherits the advantages of conventional ADRC, such as good transient performance and parameter robustness.

References

[1] G. Wang, R. Yang, and D. Xu, "DSP-based control of sensorless IPMSM drives for wide-speed range operation," *IEEE Trans. Ind. Electron.*, vol. 60, no. 2, pp. 720–727, Feb. 2013.

[2] X. Zhang, B. Wang, Y. Yu, J. Zhang, and D. Xu, "Overmodulation index optimization method for torque quality improvement in induction motor field-weakening control," *IEEE Trans. Ind. Electron.*, vol. 68, no. 12, pp. 11954–11967, Dec. 2021.

[3] X. Zhang, B. Wang, Y. Yu, J. Zhang, and D. Xu, "Minimum-nonlinear-voltage method for torque ripple suppression in induction motor overmodulation and field-weakening control," *IEEE Trans. Ind. Electron.*, vol. 69, no. 5, pp. 4495–4509, May 2022.

[4] H. Zhao, Q. M. J. Wu, and A. Kawamura, "An accurate approach of nonlinearity compensation for VSI inverter output voltage," *IEEE Trans.*

[5] D. Lee and J. Ahn, "A simple and direct dead-time effect compensation scheme in PWM-VSI," *IEEE Trans. Ind. Appl.*, vol. 50, no. 5, pp. 3017–3025, Sep./Oct. 2014.

[6] S. Q. A. Shah, T. A. Lipo, and B.-I. Kwon, "Modeling of novel permanent magnet pole shape SPM motor for reducing torque pulsation," *IEEE Trans. Magn.*, vol. 48, no. 11, pp. 4626–4629, Nov. 2012.

[7] J. Li, K. Wang, and F. Li, "Reduction of torque ripples in consequent-Pole permanent magnet machines using staggered rotor," *IEEE Trans. Energy Convers.*, vol. 34, no. 2, pp. 643–651, Jun. 2019.

[8] C. Shi, D. Li, R. Qu, H. Zhang, Y. Gao, and Y. Huo, "A novel linear permanent magnet Vernier machine with consequent-pole permanent magnets and Halbach permanent magnet arrays," *IEEE Trans. Magn.*, vol. 53, no. 11, Nov. 2017, Art. no. 2501404.

[9] A. H. Abosh, Z. Zhu, and Y. Ren, "Cascaded direct torque control of unbalanced IPMSM with low torque and flux ripples," *IEEE Trans. Power Electron.*, vol. 33, no. 2, pp. 1740–1749, Feb. 2018.

[10] M. -S. Yoo, S. -W. Park, H. -J. Lee, and Y. -D. Yoon, "Offline compensation method for current scaling gains in AC motor drive systems with three-phase current sensors," *IEEE Trans. Ind. Electron.*, vol. 68, no. 6, pp. 4760–4768, Jun. 2021.

[11] J. Han, B.-H. Kim, and S.-K. Sul, "Effect of current measurement error in angle estimation of permanent magnet AC motor sensorless control," in *Proc. IEEE 3rd Int. Future Energy Electron. Conf.*, 2017, pp. 2171–2176.

[12] Z. Tang and B. Akin, "Suppression of dead-time distortion through revised repetitive controller in IPMSM drives," *IEEE Trans. Energy Convers.*, vol. 32, no. 3, pp. 918–930, Sep. 2017.

[13] D. Li, Y. Iwaji, Y. Notohara, and K. Kishita, "Harmonic current cancellation method for IPMSM drive system using resonant controllers," in *Proc. Int. Power Electron. Conf.*, 2018, pp. 1301–1307.

[14] Z. Pan, F. Dong, J. Zhao, L. Wang, H. Wang, and Y. Feng, "Combined resonant controller and two-degree-of-freedom PID controller for PMSLM current harmonics suppression," *IEEE Trans. Ind. Electron.*, vol. 65, no. 9, pp. 7558–7568, Sep. 2018.

[15] A. H. Abosh, Z. Q. Zhu, and Y. Ren, "Reduction of torque and flux ripples in space vector modulation-based direct torque control of asymmetric permanent magnet synchronous machine," *IEEE Trans. Power Electron.*, vol. 32, no. 4, pp. 2976–2986, Apr. 2017.

[16] G. Liu, B. Chen, K. Wang, and X. Song, "Selective current harmonic suppression for high-speed IPMSM based on high-precision harmonic detection method," *IEEE Trans. Ind. Inform.*, vol. 15, no. 6, pp. 3457–3468, Jun. 2019.

[17] L. Wang, Z. Q. Zhu, H. Bin, and L. M. Gong, "Current harmonics suppression strategy for PMSM with nonsinusoidal back-EMF based on adaptive linear neuron method," *IEEE Trans. Ind. Electron.*, vol. 67, no. 11, pp. 9164–9173, Nov. 2020.

[18] Y. Luo and C. Liu, "A simplified model predictive control for a dual three-phase PMSM with reduced harmonic currents," *IEEE Trans. Ind. Electron.*, vol. 65, no. 11, pp. 9079–9089, Nov. 2018.

[19] J. Liu, H. Li, and Y. Deng, "Torque ripple minimization of PMSM based on robust ILC via adaptive sliding mode control," *IEEE Trans. Power Electron.*, vol. 33, no. 4, pp. 3655–3671, Apr. 2018.

[20] M. Huang, Y. Deng, H. Li, and J. Wang, "Torque ripple suppression of PMSM using fractional-order vector resonant and robust internal model control," *IEEE Trans. Transp. Electrific.*, vol. 7, no. 3, pp. 1437–1453, Sep. 2021.

[21] S. -Y. Kim and S.-Y. Park, "Compensation of dead-time effects based on adaptive harmonic filtering in the vector-controlled AC motor drives,"

[22] N. Urasaki, T. Senjyu, K. Uezato, and T. Funabashi, "Adaptive dead-time compensation strategy for permanent magnet synchronous motor drive," *IEEE Trans. Energy Convers.*, vol. 22, no. 2, pp. 271–280, Jun. 2007.
[23] J. Han, "From PID to active disturbance rejection control," *IEEE Trans. Ind. Electron.*, vol. 56, no. 3, pp. 900–906, Mar. 2009.
[24] J. Han, "The 'extended state observer' of a class of uncertain systems," *Control Decis.,* vol. 10, no. 1, pp. 85–87, 1995.
[25] Z. Gao, "Scaling and bandwidth-parameterization based controller tuning," in *Proc. Amer. Control Conf.*, 2003, pp. 4989–4996.
[26] Y. Xu *et al.*, "Current harmonic suppression in dual three-phase permanent magnet synchronous machine with extended state observer," *IEEE Trans. Power Electron.*, vol. 35, no. 11, pp. 12166–12180, Nov. 2020.
[27] D. Yoo, S. S.-T. Yau, and Z. Gao, "On convergence of the linear extended state observer," in *Proc. IEEE Conf. Comput. Aided Control Syst. Des.*, 2006, pp. 1645–1650.
[28] B. Guo *et al.*, "Generalized integrator-extended state observer with applications to grid-connected converters in the presence of disturbances," *IEEE Trans. Control Syst. Technol.*, vol. 29, no. 2, pp. 744–755, Mar. 2021.
[29] M. Tian, B. Wang, Y. Yu, Q. Dong, and D. Xu, "Discrete-time repetitive control-based ADRC for current loop disturbances suppression of PMSM drives," *IEEE Trans. Ind. Inform.*, vol. 18, no. 5, pp. 3138–3149, May 2022.
[30] Z. Wang, J. Zhao, L. Wang, M. Li, and Y. Hu, "Combined vector resonant and active disturbance rejection control for PMSLM current harmonic suppression," *IEEE Trans. Ind. Inform.*, vol. 16, no. 9, pp. 5691–5702, Sep. 2020.
[31] B. Wang, M. Tian, Y. Yu, Q. Dong, and D. Xu, "Enhanced ADRC with quasi-resonant control for PMSM speed regulation considering aperiodic and periodic disturbances," *IEEE Trans. Transp. Electrific.*, to be published, doi: 10.1109/TTE.2021.3138922.
[32] A. A. Godbole, J. P. Kolhe, and S. E. Talole, "Performance analysis of generalized extended state observer in tackling sinusoidal disturbances," *IEEE Trans. Control Syst. Technol.*,vol. 21, no. 6, pp. 2212–2223, Nov. 2013.
[33] X. Xie, "Stable polynomials with complex coefficients," in *Proc. 24th IEEE Conf. Decis. Control*, 1985, pp. 324–325.

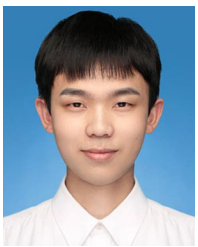

Fan Yang (Student Member, IEEE) was born in Anhui, China, in 1997. He received the B.S. degree in electrical engineering from Anhui University, Hefei, China, in 2019. He is currently working toward the M.S. degree in electrical engineering with the College of Electrical Engineering, Huazhong University of Science and Technology, Wuhan, China.

His research interests include ac motor drivers and active disturbance rejection control.

Feng Jiang (Student Member, IEEE) received the B.S. degree in electrical engineering and automation from Chongqing University, Chongqing, China, in 2016. He is currently working toward the Ph.D. degree in electrical engineering with the Huazhong University of Science and Technology, Wuhan, China.

His research interests include ac motor drivers and ac motor sensorless control.

Zhijie Xu was born in Hubei, China, in 1997. He received the B.S. degree in electrical engineering from China University of Petroleum (East China), Qingdao, China, in 2019. He is currently working toward the M.S. degree at the College of Electrical Engineering, Huazhong University of Science and Technology, Wuhan, China.

His research interests include ac motor sensorless control and active disturbance rejection control.

Lingfeng Qiu was born in Guangdong, China, in 2000. He is currently working toward the B.S. degree in electrical engineering with the College of Electrical Engineering, Huazhong University of Science and Technology, Wuhan, China.

His research interests include ac motor drivers and active disturbance rejection control.

Baichuan Xu received the B.S. degree in electrical engineering and automation from Southwest Jiaotong University, Sichuan, China, in 2019. He is currently working toward the Ph.D. degree in electrical engineering with the Huazhong University of Science and Technology, Wuhan, China.

His research interests include design and optimization of PMSM .

Yahui Zhang was born in Shanxi, China, in 1997. He received the B.S. degree in electrical engineering from Shanghai University, Shanghai, China, in 2019. He is currently working toward the M.S. degree in electrical engineering with the College of Electrical Engineering, Huazhong University of Science and Technology, Wuhan, China.

His major research interests include monitoring and evaluation of electric equipments.

Kai Yang (Member, IEEE) received the B.S., M.S., and Ph.D. degrees in electrical and electronic engineering from Huazhong University of Science and Technology, Wuhan, China, in 1998, 2000, and 2003, respectively.

He is currently a Professor and the Associate Dean with the College of Electrical and Electronic Engineering, Huazhong University of Science and Technology. His research interests include functional-material actuators, new type permanent machines, and their drive systems.